

TWO SUBCLASSES OF PROTO-PLANETARY NEBULAE: MODEL CALCULATIONS

MARGARET MEIXNER,¹ TOSHIYA UETA,¹ MATTHEW BOBROWSKY,² AND ANGELA SPECK¹

Received 2000 March 11; accepted 2002 February 8

ABSTRACT

We use detailed radiative transfer models to investigate the differences between the star-obvious low-level elongated proto-planetary nebulae (SOLE PPNs) and dust-prominent longitudinally extended proto-planetary nebulae (DUPLEX PPNs), which are two subclasses of PPNs suggested by Ueta, Meixner, & Bobrowsky. We select one SOLE PPN, HD 161796, and one DUPLEX PPN, IRAS 17150–3224, both of which are well studied and representative of their PPN classes. Using an axisymmetric dust shell radiative transfer code, we model these two sources in detail and constrain their mass-loss histories, inclination angles, and dust composition. The physical parameters derived for HD 161796 and IRAS 17150–3224 demonstrate that they are physically quite different and that their observed differences cannot be attributed to inclination-angle effects. Both HD 161796 and IRAS 17150–3224 are viewed nearly edge-on. However, the more intensive axisymmetric superwind mass loss experienced by IRAS 17150–3224 ($8.5 \times 10^{-3} M_{\odot} \text{ yr}^{-1}$ and an $\dot{M}_{\text{equator}}/\dot{M}_{\text{pole}} = 160$) has created a high optical depth dust torus ($A_V = 37$) that obscures its central star. In contrast, HD 161796, which underwent a lower rate superwind ($\dot{M} = 1.2 \times 10^{-4} M_{\odot} \text{ yr}^{-1}$ and an $\dot{M}_{\text{equator}}/\dot{M}_{\text{pole}} = 9$), has an optically thinner dust shell that allows the penetration of direct starlight. Based on our analysis of the dust composition, which is constrained by dust optical constants derived from laboratory measurements, both objects contain oxygen-rich dust, mainly amorphous silicates, but with some significant differences. IRAS 17150–3224 contains only amorphous silicates with sizes ranging from 0.001 to larger than $\sim 200 \mu\text{m}$. HD 161796 contains amorphous silicates, crystalline silicates (enstatite and forsterite), and crystalline water ice with sizes ranging from 0.2 to larger than $\sim 10 \mu\text{m}$. If these calculations reflect a more general truth about SOLE versus DUPLEX PPNs, then these two subclasses of PPNs are physically distinct, with the SOLE PPNs derived from low-mass progenitors and DUPLEX PPNs derived from high-mass progenitors.

Subject headings: planetary nebulae: general — reflection nebulae — stars: AGB and post-AGB — stars: mass loss

1. INTRODUCTION

The expulsion of a star’s outer envelope heralds the end for most stars in our galaxy. For stars such as our Sun, the observed rates at which stars lose their outer envelopes can far exceed the interior nuclear burning rates, causing these stars to wither into white dwarfs. What physical process initiates this dramatic loss of mass? Some clues to the mass-loss mechanism can come from the morphology of the ejected material. However, here lies an additional puzzle. Planetary nebulae (PNs), which are the stellar ejecta illuminated by the stellar cores that are rapidly evolving into white dwarfs (Iben 1995), appear to be mostly axially symmetric with subclasses of bipolar and elliptical morphologies (Balick 1987; Zuckerman & Aller 1986). On the other hand, the ejected circumstellar material of most asymptotic giant branch (AGB) stars, which are the precursors to PNs, appear spherically symmetric as the star sheds its envelope (Neri et al. 1998; Habing & Blommaert 1993). The morphologies of planetary nebulae are predominantly shaped by the AGB mass loss and by interaction of that mass loss with a fast wind from the evolving central star. The axisymmetry of PNs may arise when the fast wind expands a hot-gas bubble into previously ejected material that has an equatorial den-

sity enhancement (Frank & Mellema 1994). Preferential increases of density at the equator may be created by interactions of the mass loss with a binary companion (Soker 1998; Mastrodemos & Morris 1998) or with stellar rotation and a magnetic field (García-Segura et al. 1999; Blackman, Frank, & Welch 2001). Proto-planetary nebulae (PPNs), which are objects in transition from AGB stars to PNs (Kwok 1993), offer pristine fossil records of the mass-loss histories because they predate the fast-wind shaping.

Observational studies of PPN morphologies have shown that they are inherently axisymmetric (Meixner et al. 1999; Ueta, Meixner, & Bobrowsky 2000; Trammell, Dinerstein, & Goodrich 1994; Hrivnak & Kwok 1991; Su, Volk, & Kwok 2000), demonstrating that the axisymmetric structures found in PNs predate the PPN phase. Axisymmetric PN morphologies are subdivided into bipolar, elliptical, and other categories. Based on a *Hubble Space Telescope* (HST) imaging study of 27 PPNs, Ueta et al. (2000) suggest that there are two subclasses of PPNs, star-obvious low-level elongated (SOLE) and dust-prominent longitudinally extended (DUPLEX), that may be precursors to the elliptical and bipolar PNs, respectively. SOLE PPNs have prominent central stars surrounded by low surface brightness nebulae with single ellipses or sometimes multilobed structures. DUPLEX PPNs have spectacular bipolar reflection nebulae with pinched waists and no direct view or a heavily obscured view of the central star. SOLE and DUPLEX PPNs also appear to differ in three other observational categories. First, for SOLE PPNs, mid-IR images of the thermal dust emission reveal a toroidal structure embedded in a

¹ Department of Astronomy, MC-221, University of Illinois at Urbana-Champaign, Urbana, IL 61801; meixner@astro.uiuc.edu, ueta@astro.uiuc.edu, akspeck@astro.uiuc.edu.

² Challenger Center for Space Science Education, 1250 North Pitt Street, Alexandria, VA 22314; mbobrowsky@challenger.org.

TABLE 1
OBSERVED DIFFERENCES BETWEEN SOLE AND DUPLEX PPNs

Property	SOLE	DUPLEX
Optical morphology	Star + nebula	Nebula dominant
Mid-IR morphology	Toroidal	Core-elliptical
SED	Optical-far-IR	Far-IR dominant
Galactic height (pc)	$\lesssim 2100$	$\lesssim 520$

larger elliptical envelope. For DUPLEX PPNs, the mid-IR emission appears as a bright unresolved core surrounded by a low surface brightness emission (Meixner et al. 1999). Second, the spectral energy distributions (SEDs) for SOLE PPNs have roughly equal contributions from the optical and far-IR. On the other hand, in the SEDs for DUPLEX nebulae, the far-IR contribution dominates over the optical (Ueta et al. 2000; van der Veen, Habing, & Geballe 1989). Third, the Galactic scale height of the SOLE PPNs is larger than that of the DUPLEX PPNs, which appear to be more confined to the Galactic plane (Ueta et al. 2000). Corradi & Schwarz (1995) have shown a similar difference for elliptical PNs versus bipolar PNs. These differences are summarized in Table 1.

In this work, the differences between SOLE and DUPLEX PPNs are investigated using an axisymmetric radiative transfer code to model the dust shells of two PPNs. Section 2 outlines the reasoning behind our choice of objects. In § 3, we review the model calculations and results. In § 4, we compare and discuss the derived physical parameters of the two sources. Section 5 summarizes the conclusions.

2. SELECTION OF OBJECTS

In order to solidly substantiate that SOLE and DUPLEX PPNs are physically distinct PPNs as opposed to, e.g., the

same PPN viewed at different inclination angles, detailed model calculations of the entire sample of PPN would be needed. However, the computation time to accomplish such a task is substantial. The radiative transfer code that we use takes a few to a few dozen hours to compute one model run, and approximately 200 models are run in order to find a best fit. Thus, we have pursued instead a more exploratory approach of modeling one SOLE PPN and one DUPLEX PPN. In order to have the best constrained model calculations, we have selected two well-studied PPNs from the *HST* imaging sample: HD 161796, a SOLE PPN, and IRAS 17150–3224 (hereafter IRAS 17150), a DUPLEX PPN. These two PPNs share a number of properties of other PPNs in their class (§ 1; Ueta et al. 2000), and therefore it is reasonable to expect that the results for these objects will be representative of their SOLE and DUPLEX classes. These two PPNs also have some similarities. Both objects are oxygen-rich and appear to contain silicate dust grains (Justtanont et al. 1992; Kwok, Hrivnak, & Geballe 1995). Both HD 161796 and IRAS 17150 appear to be nearly edge-on from their optical and mid-IR images (Ueta et al. 2000; Meixner et al. 1999). However, their similarities end there. HD 161796, which is also known as IRAS 17436+5003, has a Galactic latitude of $30^\circ 9'$ and has most likely evolved from a thick-disk star (Luck, Bond, & Lambert 1990). IRAS 17150, on the other hand, has a Galactic latitude of $3^\circ 0'$ and is thus most certainly a population I object.

The observed properties for these two PPNs are listed in Table 2. The effective temperatures of the central stars (T_*) are based on spectral types of these stars: F3 Ib for HD 161796 (Fornie & Garrison 1984) and G2 Ia for IRAS 17150 (Hu et al. 1993). Skinner et al. (1994) derived a distance to HD 161796 of ~ 1 kpc, which is consistent with the *Hipparcos* results. The distance to IRAS 17150 is not as well known. IRAS 17150 is located in the plane of our Galaxy with a Galactic latitude and longitude of $3^\circ, 354^\circ$, and thus we can assign a kinematic distance. Using its systemic velocity of ~ 15 km s $^{-1}$ (Hu et al. 1993), we find a distance of 3.6

TABLE 2
PROPERTIES OF THE TWO SELECTED PPNs FROM OBSERVATIONS AND BEST-FIT MODELS

Quantity	HD 161796	IRAS 17150–3224	Reference
$L_* \propto d^2 (L_\odot)$	2800	27200	
T_* (K) ($\pm 10\%$)	7000	5200	1, 2
$R_* \propto d^2 (R_\odot)$	34	201	
d (kpc)	1.0	3.6	3, 4
ISM A_V	0.0	0.8	5
$T_{\text{dust at } R_{\text{min}}}$ (K)	110	220	
$R_{\text{min}} \propto d (10^{15} \text{ cm})$	11	9.7	
v_{exp} (km s $^{-1}$)	12.0	15.0	2, 6
i (deg)	90 ± 30	82 ± 8	
A_V at pole	0.80	0.98	
A_V at equator	1.4	37	
Shell mass $\propto d^2 (M_\odot)$	2.0	14.0	7
$\dot{M}_{\text{AGB}} \propto d^2 (10^{-4} M_\odot \text{ yr}^{-1})$	1.2	5.3	7
$t_{\text{AGB}} \propto d (10^4 \text{ yr})$	1.7	2.0	
$\dot{M}_{\text{SW}} \propto d^2 (10^{-4} M_\odot \text{ yr}^{-1})$	1.2	85	7
$t_{\text{SW}} \propto d$ (yr)	590	410	
$t_{\text{dyn}} \propto d$ (yr)	300	210	
$\dot{M}_{\text{equator}} / \dot{M}_{\text{pole}}$	9	160	

REFERENCES.—(1) Hrivnak et al. 1989; (2) Hu et al. 1993; (3) Skinner et al. 1994; (4) this work; (5) Neckel et al. 1980; (6) Likkell et al. 1987; (7) assumed gas-to-dust mass ratio of 280 from Justtanont et al. 1996.

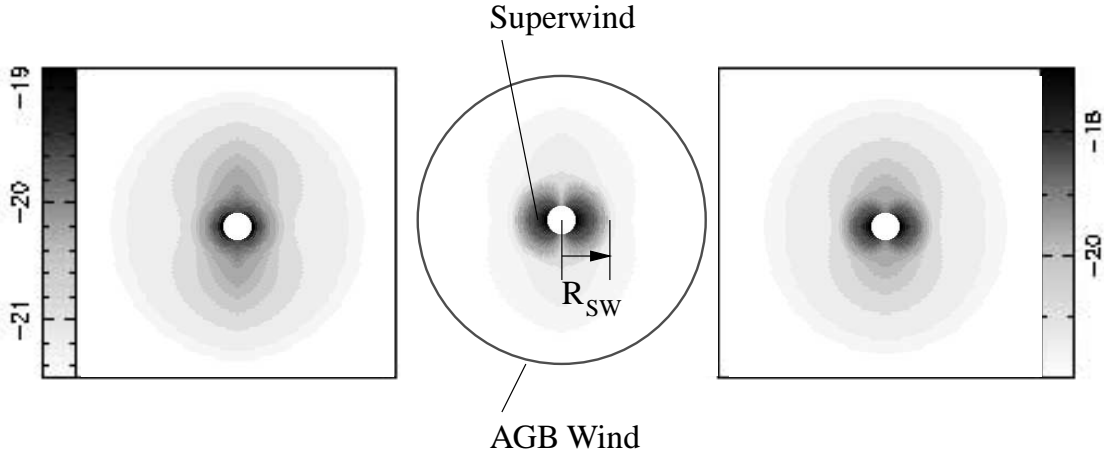


FIG. 1.—Gray-scale schematics of the PPN density function used in the model calculations. The gray-scale wedges are in units of g cm^{-3} . The central diagram shows the locations of the axisymmetric superwind and spherically symmetric AGB wind with R_{SW} as the boundary. The inner radius, R_{min} , and the outer radius, R_{out} , define the inner and outer boundaries of this density function. The left image shows the density function used in the model of HD 161796. The right image shows the density function used in the model of IRAS 17150.

kpc using the rotation curve information derived from H I observations (Burton 1988). This kinematic distance seems reasonable in light of the resemblance that IRAS 17150 bears to AFGL 2688 (Kwok, Su, & Hrivnak 1998), which has an estimated distance of ~ 1.2 kpc (Skinner et al. 1997). If we assume that IRAS 17150 and AFGL 2688 have comparable luminosities, then we estimate a distance of 3.6 kpc for IRAS 17150 by comparing their bolometric fluxes. Extinction due to interstellar dust was estimated from the work of Neckel, Klare, & Sarcander (1980). The expansion velocities, v_{exp} , are based on CO observations. We note, however, that for IRAS 17150, the CO observations show a larger expansion velocity of 15 km s^{-1} compared to the 6 km s^{-1} of the 1665 MHz OH masers, and thus the actual expansion velocity is uncertain as a result of velocity gradients in this source (Hu et al. 1993), but the CO observations will be adequate for our comparison of the two objects.

3. AXISYMMETRIC MODELS

For our modeling, we use a dust radiative transfer code, called **2-DUST**. The computation method is based on the iterative scheme devised by Collison & Fix (1991) and follows the principle of long characteristic. It will be discussed in detail by T. Ueta & M. Meixner (2002, in preparation). In these calculations, the central star illuminates an axisymmetric circumstellar dust shell, and the dust shell reddens and scatters the starlight. Self-consistency is achieved through requiring global luminosity constancy at each radial grid point in the dust shell. The density function of the dust shell is of central interest to this work because it is directly related to the mass-loss history of the object. Here, we have adopted a density function that can have a toroidal interior, an elliptical (prolate or oblate) mid-region, and a spherical outer shell. This function embodies the idea that the mass-loss rate was spherically symmetric on the AGB (M_{AGB}) and became axisymmetric during the superwind phase (M_{SW}). The density functions used in our calculations

are shown in Figure 1 and have the following form:

$$\rho(R, \theta) = \rho_{\text{min}} \left(\frac{R}{R_{\text{min}}} \right)^{-B} \left\{ 1 + C \sin^F \theta \left[e^{-(R/R_{\text{SW}})^D} / e^{-(R_{\text{min}}/R_{\text{SW}})^D} \right] \right\} \\ \times \left\{ 1 + A(1 - \cos \theta)^F \left[e^{-(R/R_{\text{SW}})^E} / e^{-(R_{\text{min}}/R_{\text{SW}})^E} \right] \right\}, \quad (1)$$

$$R_{\text{min}} < R < R_{\text{max}},$$

where $\rho(R, \theta)$ is the dust-grain mass density at radius R and latitude θ , ρ_{min} is the dust-grain mass density on the polar axis at the inner edge of the envelope, R_{min} is the inner radius of the shell, R_{max} is the outer radius of the shell, and R_{SW} is the boundary between the spherical AGB wind and the axisymmetric superwind. The first term, R/R_{min}^{-B} , defines the radial profile of the spherical AGB wind. The $[1 + C \dots]$ term that follows B in the exponent defines the elliptical mid-shell. The second term, $[1 + A \dots]$, defines the equatorial enhancement of the superwind. The user-defined constants, A – F , define the density profile. The degree of equatorial enhancement is set by A , where $1 + A$ is the equator-to-pole density ratio at R_{min} , and C , where the density drop with radius along the equator is steepened by a factor of $(1 + C)$. The inner torus can be made torus-like or disk-like with F , while D and E define the mid-shell region oblate or prolate.

Figure 1 also shows the two-dimensional density functions used in our “best-fit” models of HD 161796 and IRAS 17150. The user-defined constants for the model density functions are listed in Table 3. The ρ_{min} is determined by the user-specified optical depth at the equator of the dust shell at a specific wavelength and is listed in Table 3 as $\tau_{9.8 \mu\text{m}}$ at equator.

The properties of the dust grains are also constrained by our modeling. For the grain-size distribution, we assume a power law plus exponential falloff,

$$a^{-3.5} e^{-a/a_0}, \quad a_{\text{min}} < a < \infty, \quad (2)$$

for which a minimum grain size a_{min} and an effective maxi-

TABLE 3
PARAMETER VALUES FOR THE DENSITY FUNCTIONS OF
BEST-FIT MODELS

Parameter	HD 161796	IRAS 17150–3224
<i>A</i>	8	159
<i>B</i>	2	2
<i>C</i>	2	1.5
<i>D</i>	1	1
<i>E</i>	3	4
<i>F</i>	1	1.5
$\tau_{9.8\ \mu\text{m}}$ at equator.....	0.46	12.0
$\tau_{9.8\ \mu\text{m}}$ at pole.....	0.26	0.32

imum grain size a_0 are specified and for which the number of grains larger than a_0 is diminishingly small (Kim, Martin, & Hendry 1994). This grain-size distribution was derived for the interstellar medium (ISM) and may or may not be appropriate for circumstellar grains. A theoretical study by Dominik, Sedlmayr, & Gail (1989) suggests that the grain-size distribution created in the circumstellar environments of AGB stars has a steeper power law (a^{-5}); however, this parameter has yet to be studied observationally. The absorption and scattering cross sections are calculated for each wavelength using Mie theory and dust optical constants derived from laboratory measurements. For the radiative transfer, we consider a fiducial grain that has size- and composition-averaged cross sections at each wavelength (Ueta et al. 2001a). Table 4 lists the dust properties for each source. In a detailed study of HD 161796's mineralogy, Hoogzaad et al. (2002) have determined that amorphous silicates ($\text{Mg}_{0.5}\text{Fe}_{0.5}\text{SiO}_4$, olivine; Dorschner et al. 1995), water ice (Warren 1984; Bertie, Labbé, & Whalley 1969), crystalline forsterite (Scott & Duley 1996; Servoin & Piriou 1973), and crystalline enstatite (Scott & Duley 1996; Jaeger et al. 1998) are all present in the circumstellar dust shell. Thus, we include all four dust species in our model. For IRAS 17150, however, we needed only amorphous silicates ($\text{Mg}_{0.5}\text{Fe}_{0.5}\text{SiO}_4$, olivine; Dorschner et al. 1995).

We approached the modeling by starting simply and increasing complexity as demanded by the observations. The SEDs are fitted first and these constrain the dust opacity ($\tau_{9.8\ \mu\text{m}}$), dust grain composition, luminosity (L_*), stellar and dust temperatures (T_* , T_{dust}) and inner radius of the dust shell (R_{min}). The optical and mid-IR images constrain R_{min} , $\tau_{9.8\ \mu\text{m}}$, the inclination angle (i), and density function parameters *A–F*. Approximately 300 models were run for IRAS 17150 and 150 models were run for HD 161796 before convergence on a best-fit model. We have used earlier ver-

TABLE 4
DUST PROPERTIES FOR BEST-FIT MODELS

Quantity	HD 161796	IRAS 17150–3224	Reference
a_{min} (μm).....	0.2	0.001	
a_0 (μm).....	10.0	200.0	
Amorphous silicate.....	86.5%	100%	1
Crystalline enstatite.....	6%	0%	2, 3
Crystalline forsterite.....	5%	0%	2, 4
Water ice.....	2.5%	0%	5, 6

REFERENCES.—(1) Dorschner et al. 1995; (2) Scott & Duley 1996; (3) Jaeger et al. 1998; (4) Servoin & Piriou 1973; (5) Warren 1984; (6) Bertie et al. 1969.

sions of this code to model several objects (Meixner et al. 1997; Skinner et al. 1997; Ueta et al. 2001a, 2001b). We refer the reader to Ueta et al. (2001b), Skinner et al. (1997), and Appendix A of Meixner et al. (1997) for further details on the modeling procedure, and to Ueta et al. (2001a) for details on the effects of a grain-size distribution.

In the following sections, we compare the model SED with spectra and photometry and model images with data images for our two sources, HD 161796 and IRAS 17150. The photometry, spectroscopy, and image data are taken from the literature. The derived stellar and dust-shell parameters from the models are listed in Table 2. The model images have the same pixel scale as the observed images. The model mid-IR images are convolved with a Gaussian point-spread function (PSF) that has an FWHM equivalent to the observed FWHM of the mid-IR images. The model optical images did not require smoothing for comparison with the *HST* images.

3.1. HD 161796

Previous model calculations for HD 161796 have assumed spherical symmetry (Hrivnak, Kwok, & Volk 1989; Skinner et al. 1994; Hoogzaad et al. 2002) and have concentrated on fits to the SED, while here we present the first axisymmetric model for this source and make detailed comparisons with images and the SED. We compare the data and model results for HD 161796 with images (Fig. 2) and SED (Fig. 3). The best-fit model has an inclination angle of 90° (see Tables 2, 3, and 4 for other model parameters). Looking at the images of HD 161796, one can see how the SED is formed. The bright central star outshines the low-level elliptical reflection nebula in the optical (Fig. 2). Both the central star and reflection nebula contribute significantly to the prominent optical peak in the SED (Fig. 3). The contours of $12.5\ \mu\text{m}$ emission show the distribution of thermal radiation from the dust grains and reveal a round dust nebula with two limb-brightened peaks located on either side of the central star, indicative of an edge-on, optically thin dust torus (Fig. 2; Skinner et al. 1994). An image at $8.5\ \mu\text{m}$ from Skinner et al. (1994) shows that the central star is located at the center of the dust nebula and is used for registration of the *V*-band and $12.5\ \mu\text{m}$ images. The dust shell is responsible for the far-IR peak in the SED (Fig. 3), and the mid-IR emission shown in Figure 2 arises from the inner edge of this dust shell.

The model images compare reasonably well with the data images (Fig. 2). In particular, the star is visible among the reflection nebula, even in this edge-on configuration. The model mid-IR emission nebula has a separation of the two limb-brightened peaks that matches the data exactly. Indeed, the separation of the two peaks provides a tight constraint on R_{min} . The model optical reflection nebula has a comparable relative brightness to the central star, as shown by the *HST* images. The model image reproduces the elliptical shape of the observed reflection nebula but extends to a larger radius than observed and appears more rounded in the outer radii. While *HST*'s Wide Field Planetary Camera 2 PSF halo could hide a faint spherical halo around the elliptical reflection nebula, the model images are not a perfect match to the data. In an optically thin nebula, the mid-IR traces the location of the warm dust, and the optical reflection nebula traces the location of the dust near the central star where densities and optical light intensities are

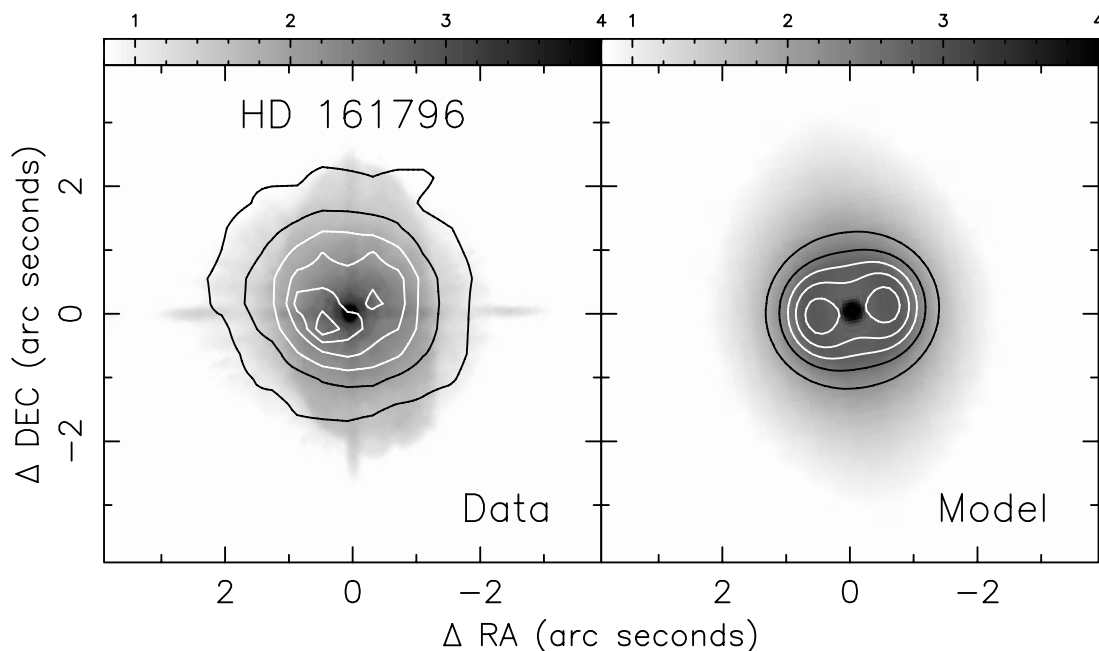


FIG. 2.—Data (*left*) and model (*right*) images for HD 161796. The contours show the thermal dust emission at $12.5\ \mu\text{m}$. Contour levels are 10%, 30%, 50%, 70%, and 90% (82.5% and 90% for data) of the peak. Peak values are $0.95\ \text{Jy arcsec}^{-2}$ for the data and $2.08\ \text{Jy arcsec}^{-2}$ for the model. The gray-scale image shows the scattered and direct starlight at V band ($0.55\ \mu\text{m}$) displayed in log-scaled intensity units of mJy pixel^{-1} , where the pixel scale is $0''.023$ and $0''.046$ for data and model, respectively. The *HST* V -band image, which shows the diffraction spikes in its PSF, is from Ueta et al. (2000), and the $12.5\ \mu\text{m}$ image is from Skinner et al. (1994).

highest. Thus, some of the slight differences between the model and data images suggest some slight differences between the model and the actual dust-density distribution. For example, the two peaks in the mid-IR nebula are rotated approximately 25° compared to the model, and the eastern peak is slightly brighter than the western peak, whereas the model shows both peaks at an equal brightness. This unevenness suggests a slight asymmetry in the axisymmetric dust density distribution or perhaps that the central

star is off center and heating the eastern portion to a hotter temperature. Secondly, the mid-IR nebula is more extended than the model nebula, which may be in part due to the PSF being non-Gaussian. However, a larger mid-IR nebula may be produced if the density dropoff is slower than our model assumes.

Drastically changing the inclination angle to our line of sight only worsens the fit to the images. Figure 4 shows model images for our best-fit model at inclination angles from 0° to 90° . As our view of the nebula changes from edge-on (90°) to pole-on (0°), the optical reflection nebula changes from an elliptical shape to a circular shape, and the two limb-brightened peaks in the mid-IR emission nebula become broader and fade into a circular ring. While a 90° inclination angle fits the SED and images best, we find that an inclination angle as low as 60° would provide an adequate fit to the data images. Thus, we include an error bar of $\pm 30^\circ$.

The model SED is in good agreement with the photometry and *Infrared Space Observatory* (*ISO*) spectrum of this source (Fig. 3), and the SED fit is better than, e.g., that of Skinner et al. (1994). The *ISO* spectrum (Molster 2002a) and the model calculations of Hoogzaad et al. (2002) have much better spectral resolution than our model. Consequentially, our model shows only the gross dust features such as the broad amorphous silicate bands at 10 and $18\ \mu\text{m}$ and the water ice feature at $43\ \mu\text{m}$. The crystalline silicate features due to forsterite and enstatite (24 and $34\ \mu\text{m}$), which are reproduced by Hoogzaad et al. (2002), are not reproduced by our model because of the coarse sampling of wavelengths. The near-IR radiation is slightly overestimated by our model because the model water ice absorption features in the near-IR (3 , 4.6 , and $6\ \mu\text{m}$) are too shallow. Our assumed mass fraction of water ice, 2.5% , is substan-

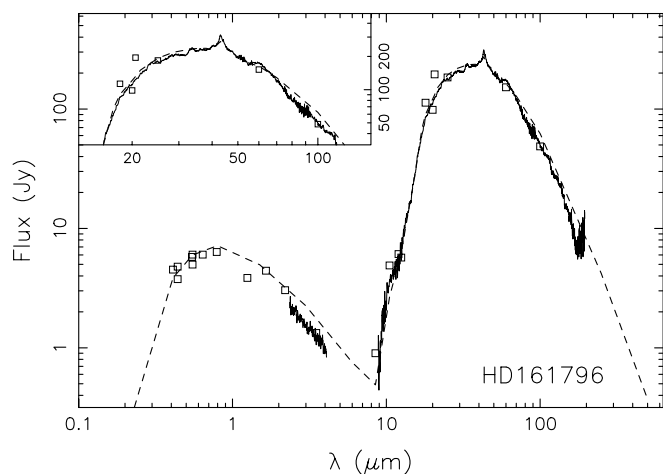


FIG. 3.—SED of HD 161796. The model calculated SED is shown in dashed lines. The *ISO* mid-IR spectrum (*solid line*) is from Molster et al. (2002a) and Hoogzaad et al. (2002). The photometry data (*squares*) are from a compilation by Ueta et al. (2000), which includes data from Humphreys & Ney (1974), Fernie (1983), Hrivnak et al. (1989), Skinner et al. (1994), Meixner et al. (1999), Ueta et al. (2000), and *IRAS*. The inset shows the IR peak around $40\ \mu\text{m}$.

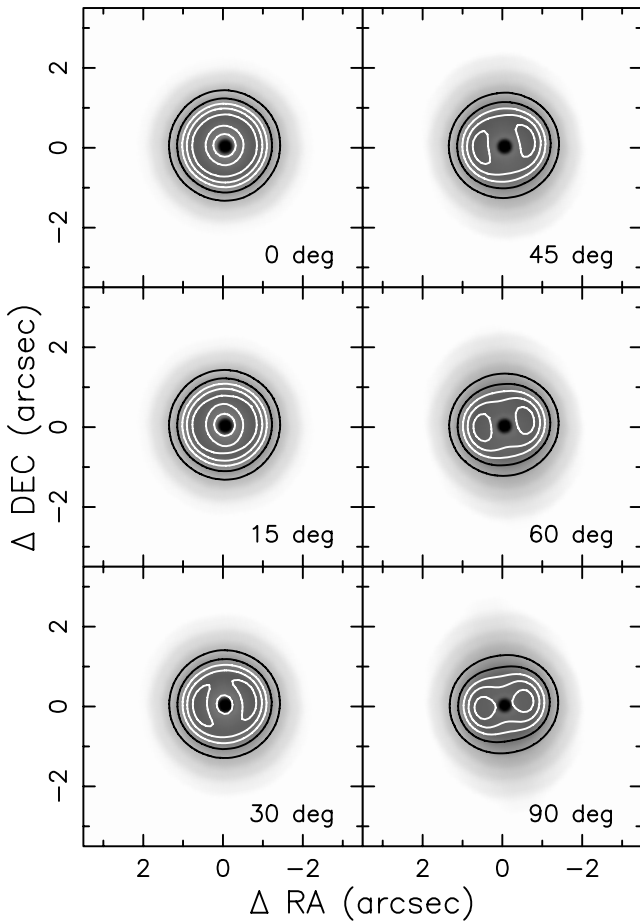


FIG. 4.—Model images for HD 161796 shown at inclination angles 0° – 90° . The contours show the thermal dust emission at $12.5 \mu\text{m}$, and the gray-scale shows the optical V -band images.

tially less than that of Hoogzaad et al. (2002), who found 24%. In the model of Hoogzaad et al. (2002), most of the water ice exists as a mantle on amorphous silicate grains that are cooler than the grains in our model, and this dust model causes the mass fraction of water ice to be quite high. In our model calculations, we found that the $43 \mu\text{m}$ water ice feature was too pronounced with a 24% mass fraction. However, the near-IR flux levels were better fitted with a 24% mass fraction of water ice. The mid-IR flux (20 – $40 \mu\text{m}$) is slightly overestimated, but a higher spectral resolution may resolve this excess into the crystalline silicate features.

The differences between our model results and previous work is in part due to our use of an axisymmetric model, but also in part due to the differences in grain parameters. Skinner et al. (1994) used the astronomical silicate (Draine & Lee 1984) and a Mathis, Rumpl, & Nordsieck (1977) grain-size distribution. Hrivnak et al. (1989) used the silicate opacity function of Volk & Kwok (1988) in their calculations. Hoogzaad et al. (2002) have made the most detailed analysis of the grain mineralogy to date. They follow the radiative transfer of each grain size and type separately, allowing a more careful analysis of grain composition than our averaged grain properties approach permits.

When rescaled appropriately for differences in assumed distance, our derived physical parameters are comparable to Skinner et al. (1994) but significantly different from those of Hrivnak et al. (1989). While our luminosity

($L_* \sim 2800 L_\odot$) and R_{min} ($11 \times 10^{15} \text{ cm}$) are within 30% of Skinner et al. (1994), our mass-loss rates ($1.2 \times 10^{-4} M_\odot \text{ yr}^{-1}$) are a factor of 2 lower than those of Skinner et al. (1994). The reason for this difference is most likely the difference in dust parameters. Our grain sizes (0.2 – $10.0 \mu\text{m}$) are significantly larger than those assumed by Skinner et al. (0.005 – $1.0 \mu\text{m}$). Larger grains are more efficient at emitting far-IR radiation, and thus our models require less dust mass to create the observed far-IR radiation. The R_{min} , luminosity, and mass-loss rates derived by Hrivnak et al. (1989) are all significantly larger than our values. The predicted R_{min} value of $2.8 \times 10^{16} \text{ cm}$ by Hrivnak et al. (1989) is not consistent with the mid-IR image of Skinner et al. (1994). This large value for R_{min} probably forced the value for L_* higher to create a high enough dust temperature to match the IR emission. However, in order to match the optical part of the SED, Hrivnak et al. (1989) had to include some extinction due to the ISM ($A_V = 0.7$), which was not needed by our model or the model of Skinner et al. (1994) and is not supported by measurements of ISM extinction in the direction of this object (Neckel et al. 1980). This comparison demonstrates the importance of imaging for independent constraints of the R_{min} parameter.

3.2. IRAS 17150–3224

We compare the data and model results for IRAS 17150 with images (Fig. 5) and SED (Fig. 6). The best-fit model has an inclination angle of 82° (see Tables 2, 3, and 4 for other model parameters). In contrast to HD 161796, the central star of IRAS 17150 is completely obscured by the optically thick dusty torus. Instead, we see a spectacular bipolar reflection nebula in the B -band image (Fig. 5). The bipolar reflection nebulosity is the only contributor to the small amount of optical emission in the SED (Fig. 6). Contours of $9.8 \mu\text{m}$ emission show the distribution of thermal radiation from the silicate dust grains and reveal a compact, elliptical dust nebula associated with the optically obscured region (Fig. 5; Meixner et al. 1999). The accuracy of this optical and mid-IR registration is limited by the absolute position of the mid-IR image, which is known to about $1''$; however, it is reasonable to assume that the mid-IR peak is associated with the optically obscuring dusty disk. This mid-IR emission traces the inner regions of the dust shell, which extends beyond the optical reflection nebulosity. This dust shell, particularly its inner region, absorbs almost all of the starlight and reemits it in the infrared. Hence, the infrared radiation from this dust dominates the SED of IRAS 17150 (Fig. 6).

The model images reproduce the spectacular bipolar reflection nebula and the absence of the central star (Fig. 5). In particular, the size, basic shape, and gap between the lobes are well reproduced, although the model image intensity is higher in the central region compared to the data image. We did not attempt to reproduce the fascinating arcs observed in this source (Kwok et al. 1998). The model mid-IR emission is extended but slightly smaller than that observed, in part because a Gaussian PSF does not sufficiently model the wings of the actual mid-IR PSF. The slight discrepancies between the model and data images may indicate slight differences between the assumed and actual dust-density distribution. Our fit to the optical reflection nebulosity is slightly better than the fit derived by Su et al. (2000), which has triangular-shaped lobes as opposed to the

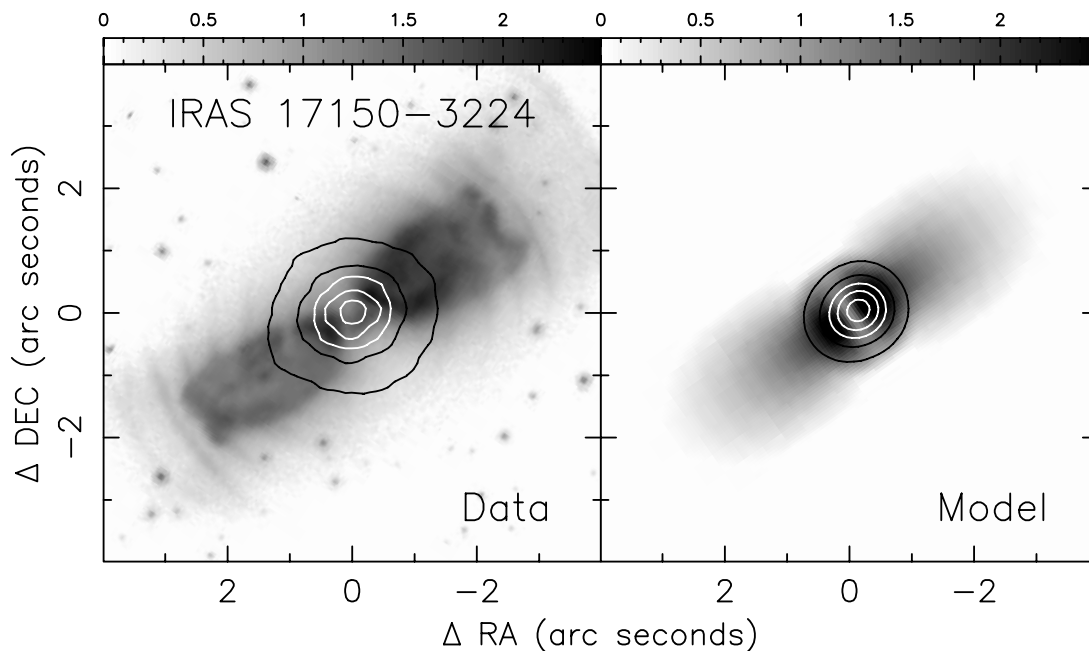


FIG. 5.—Data (left) and model (right) images for IRAS 17150–3224. The contours show the thermal dust emission at $9.8 \mu\text{m}$. Contour levels are 20%, 30%, 50%, 70%, and 90% of the peak. Peak values are $27 \text{ Jy arcsec}^{-2}$ for the data and $39.3 \text{ Jy arcsec}^{-2}$ for the model. The gray-scale images show the reflection nebula at the B band ($0.45 \mu\text{m}$) displayed in log-scaled intensity units of mJy pixel^{-1} , where the pixel scale is $0''.023$ and $0''.046$ for data and model, respectively. The B -band HST image is from Ueta et al. (2000), and the $9.8 \mu\text{m}$ is from Meixner et al. (1999).

observed rectangular shape. The differences in our model images are due mostly to our different adopted density distributions.

The images and SED we display here are for an inclination angle of 82° , which seems to fit the differences in reflection lobe brightnesses (Su et al. 2000). Figure 7 shows model images for our best-fit model at inclination angles from 0°

to 90° . As our view of the nebula changes from edge-on (90°) to pole-on (0°), the optical image transforms from a bipolar nebula with no central star ($60^\circ, 90^\circ$) to a bipolar nebula with a central star ($30^\circ, 45^\circ$) to an elliptical or circular nebula with a central star ($0^\circ, 15^\circ$). On the other hand, the mid-IR emission changes from a marginally resolved elliptical nebula extended along the bipolar nebula to an unresolved point source ($\leq 60^\circ$). Comparison of our model images with the data suggest that inclination angles in the range of 74° – 90° could provide an adequate fit, and thus we include an error bar of $\pm 8^\circ$ for the inclination angle.

The model SED compares well with the photometry and spectroscopy data (Fig. 6); in particular, the silicate absorption feature at $9.8 \mu\text{m}$ is well fitted. The added ISM extinction of $0.8A_V$, which is consistent with the measurements of Neckel et al. (1980), improves the fit to the optical photometry. The model fits the highest points of the near-IR photometry; however, we note that there is a large scatter in these data, some of which may be due to systematic errors because IRAS 17150 is in a crowded field. The near-IR light is created mostly by scattered starlight, and the excess of this light may indicate that the dust optical properties, which are derived from lab measurements of real silicates, produce too much scattering. While reasonable, the far-IR fit is slightly high at $100 \mu\text{m}$ and slightly low at 1.3 mm . In our model, the submillimeter excess of this source observed by Hu et al. (1993) is created by warm, extremely large dust grains of $\sim 200 \mu\text{m}$ in radius in the high-density torus near the central star. Figure 6 shows how the SED changes when one modifies the number of large grains by decreasing a_0 from 200 to $10 \mu\text{m}$ while keeping all other parameters the same. With $a_0 = 10 \mu\text{m}$, the submillimeter flux is significantly underestimated. Because we included the large dust grains in our model calculations, we are able to match the flux of submillimeter photometry points where previous models under-

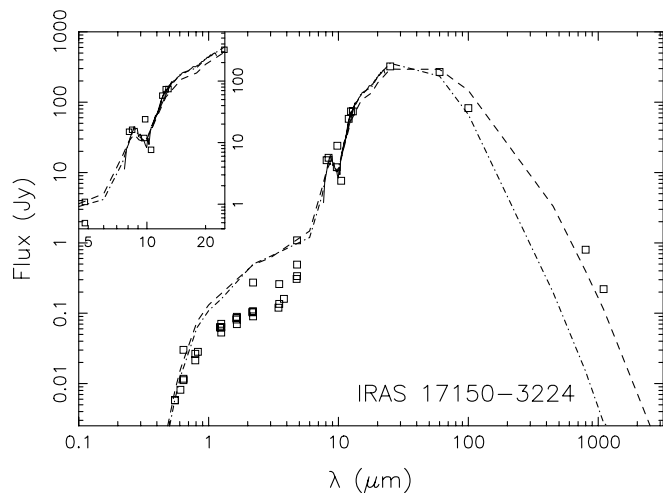


FIG. 6.—SED of IRAS 17150–3224. The model calculated SED is shown in dashed lines ($a_0 = 200 \mu\text{m}$). The mid-IR spectra are from Kwok et al. (1995; solid lines) from the *IRAS* Low Resolution Spectrometer. The photometry data (squares) are from the compilation of several sources by Ueta et al. (2000), which include data from van der Veen et al. (1989), Hu et al. (1993), Kwok et al. (1996), Reddy & Parathasarathy (1996), Meixner et al. (1999), Ueta et al. (2000), and *IRAS*. The inset shows a close-up of the $9.8 \mu\text{m}$ silicate absorption feature. The dot-dashed line represents another model with $a_0 = 10 \mu\text{m}$, which shows the dependence of far-IR and submillimeter continuum emission on larger grain sizes.

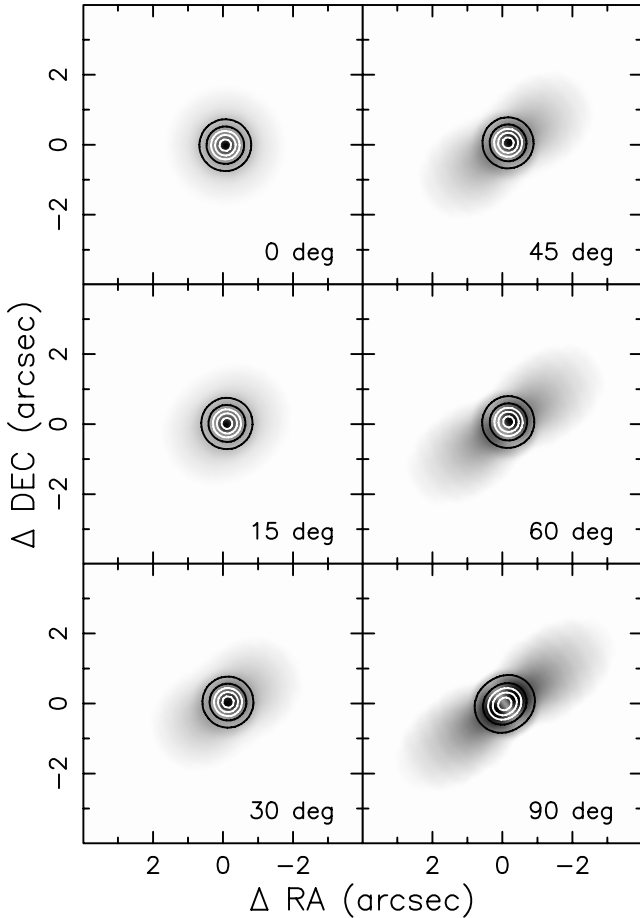


FIG. 7.—Model images for IRAS 17150–3224 shown at inclination angles 0° – 90° . The contours show the thermal dust emission at $9.8 \mu\text{m}$, and the gray scale shows the optical B -band images.

estimated the flux (Su et al. 2000; Hu et al. 1993). Moreover, our match to the optical photometry is better than previous modeling efforts. Hu et al. (1993) employed a spherically symmetric model that does not allow any optical light to escape in a bipolar reflection nebula and therefore severely underestimates the optical light. The model SED of Su et al. (2000) has a double-peaked structure with one peak at $1 \mu\text{m}$, which is quite different than the flattened rolled structure of the observed SED at the optical wavelengths. The grain properties adopted by Su et al. (2000) are different from ours, which probably explains most of the difference in our model SEDs.

When corrected for differences in distance, our model luminosity ($L_* \sim 27, 200 L_\odot$) is within 10% of that derived by Hu et al. (1993); however, the other parameters are significantly different. Our inner radius ($R_{\text{min}} \sim 9.7 \times 10^{15} \text{ cm}$) is a factor of 2 larger than Hu et al. (1993) and our dust temperature at R_{min} ($T_{\text{dust}} = 222 \text{ K}$) is consequentially lower. The latter two parameters are well constrained by the mid-IR image in combination with the SED. The mass-loss rate derived by Hu et al. (1993; $3 \times 10^{-4} M_\odot \text{ yr}^{-1}$) is comparable to our derived AGB mass-loss rate ($5.3 \times 10^{-4} M_\odot \text{ yr}^{-1}$) but significantly smaller than our derived superwind mass-loss rate ($8.5 \times 10^{-3} M_\odot \text{ yr}^{-1}$). Since our model is a better fit to the data than Hu et al. (1993), the differences in mass-loss rates reflect the refinement of our model, especially the axisymmetric geometry, over their more simple model.

4. DISCUSSION

Comparing the images and SEDs of HD 161796 and IRAS 17150, one can see that they are quite different. The derived parameters from the model calculations listed in Table 2 give us some insight as to why they look different. The basic geometry used to model both objects is the same: the difference lies in the chosen physical parameters for the dust shells. Interestingly, both objects have similar, nearly edge-on inclination angles. However, they do differ in optical depth of the dust, mass-loss history, and dust-grain composition.

4.1. Mass-Loss Histories

The apparent differences between HD 161796 and IRAS 17150 can be explained straightforwardly by differences in their mass-loss histories derived in our model calculations (see Table 2). Both objects ended their lives on the AGB with an axisymmetric superwind. However, every quantity related to the mass loss for IRAS 17150 is significantly higher than for HD 161796. IRAS 17150's superwind mass-loss rate, \dot{M}_{sw} , is a factor of 100 larger than that of HD 161796, while its AGB wind mass-loss rate, \dot{M}_{AGB} , is a factor of 5 higher than that of HD 161796. For IRAS 17150, there is a factor of 16 increase in mass-loss rate between the AGB wind and the superwind, but there is essentially no average increase for HD 161796—just a change in geometry. Note that the superwind mass-loss rates quoted in Table 2 are latitude-averaged and that the equatorial mass-loss rate is much more intensive than the polar mass-loss rate. Thus, the equatorial mass-loss rate for HD 161796 is much higher during the superwind phase than during the AGB wind phase. During the superwind, the equator-to-pole mass-loss ratio is 160 for IRAS 17150 and only 9 for HD 161796. While the mass-loss rates for IRAS 17150 were higher than for HD 161796, the durations of the superwind and AGB winds are comparable. Thus, the higher optical depth for IRAS 17150 compared to HD 161796 is caused by the more intensive mass loss experienced by IRAS 17150, particularly during the superwind phase as it ended its life on the AGB. The absolute values for these mass-loss rates depend on the gas-to-dust mass ratio and the distance to the object. We adopt a gas-to-dust mass ratio of 280 derived for the OH/IR star OH 26.5+0.6 by Justtanont et al. (1996). However, it should be noted that gas-to-dust mass ratios vary by several factors for O-rich AGB stars (Habing 1996). If IRAS 17150 were actually closer than 3.6 kpc, then the mass-loss rates would be smaller than calculated because mass-loss rates depend on the square of the distance. However, IRAS 17150 cannot be as close as HD 161796 because then its luminosity would be smaller than that of HD 161796, which is inconsistent with IRAS 17150 being a Population I object and HD 161796 being a thick-disk object. It could also not be too close because then the mass-loss rates for IRAS 17150 would be so low compared to HD 161796 that it would be hard to explain the silicate-absorption feature in IRAS 17150. Hence, despite uncertainties in distances, the mass-loss rates for IRAS 17150 must have been higher than they were for HD 161796.

The total mass for the circumstellar shell of IRAS 17150, $14.0 M_\odot$, is substantially higher than the mass for HD 161796, $2.0 M_\odot$. This difference in circumstellar mass points to a difference in progenitor-star mass. If we assume that the central star masses are $\sim 0.6 M_\odot$ for HD 161796 and

$\sim 1.0 M_{\odot}$ for IRAS 17150 (Iben & Renzini 1983), then IRAS 17150's progenitor star was much more massive than HD 161796's, in agreement with their Population I versus thick-disk classes. We note that the total mass for IRAS 17150 ($15 M_{\odot}$) is higher than typically expected for an intermediate-mass star. Given the uncertainties in the gas-to-dust mass ratio and distance for this source, we do not place great significance on this high number; however, clearly IRAS 17150 must be on the high-mass end of stars that evolve into PNs and white dwarfs.

4.2. Inclination Angle Effects

Comparison of Figures 4 and 7 shows clearly that one cannot view the model for HD 161796 at any inclination angle and see something like IRAS 17150. However, one might be tempted to think that one could view the IRAS 17150 model pole-on, where the optical depth is low, and see something like HD 161796. To test this idea, we have redisplayed the 0° and 15° inclination angles for the IRAS 17150 model in Figure 8 to show the appearance of the structure if the nebula were at a distance of 1 kpc. These images provide a reasonably accurate comparison with HD 161796 because the R_{\min} of the two sources are comparable in our models, and thus the ability to resolve R_{\min} would be the same if the objects were at the same distance.

The images in Figure 8 do not look like the data images for HD 161796 (Fig. 2) and are a considerably poorer match than our optically thin model for HD 161796. The 0° inclination angle (Fig. 8) provides a better match to the optical data than the 15° because the central star is centrally located, as observed; however, the reflection nebula is perfectly round and has none of the observed ellipticity. Moreover, the mid-IR emission for the 0° image is perfectly round and does not show the two limb-brightened peaks. The optical 15° image (Fig. 8) reveals more emission on the northwest side of the star, making the central star appear off-center. The mid-IR 15° image shows a similar asymmetry to the optical image with one peak located to the northwest of the central star location at $(0'', 0'')$. These asymmetries are created by the high optical depths at optical and $9.8 \mu\text{m}$. The peak in the mid-IR arises from the warm dust emission on the hotter, inner edge of the optically thick dust torus, which we observe through the northwest biconal opening that is pointing toward us. The optical depth in the mid-IR for this source is simply too high to see two limb-brightened peaks.

Thus, the difference in appearance cannot be attributed to an inclination angle effect where HD 161796 is viewed pole-on and IRAS 17150 is viewed edge-on. Rather, we can see the central star of HD 161796, whereas the central star of IRAS 17150 is invisible because the dust optical depth along the equatorial plane for HD 161796, $A_V = 1.4$, is substantially smaller than for IRAS 17150, $A_V = 37$.

This discussion demonstrates the importance of images in differentiating inclination-angle effects and dust-shell optical-depth effects. In particular, well-resolved mid-IR emission images can clearly distinguish between a nearly edge-on optically thin model and a nearly pole-on optically thick model where just SEDs alone cannot. Optically thin, nearly edge-on PPNs will show two peaks symmetrically centered on the star. Optically thick, nearly pole-on PPNs will show one asymmetric peak or a nearly complete circle.

While inclination-angle effects do not explain the differences between HD 161796 and IRAS 17150, they are impor-

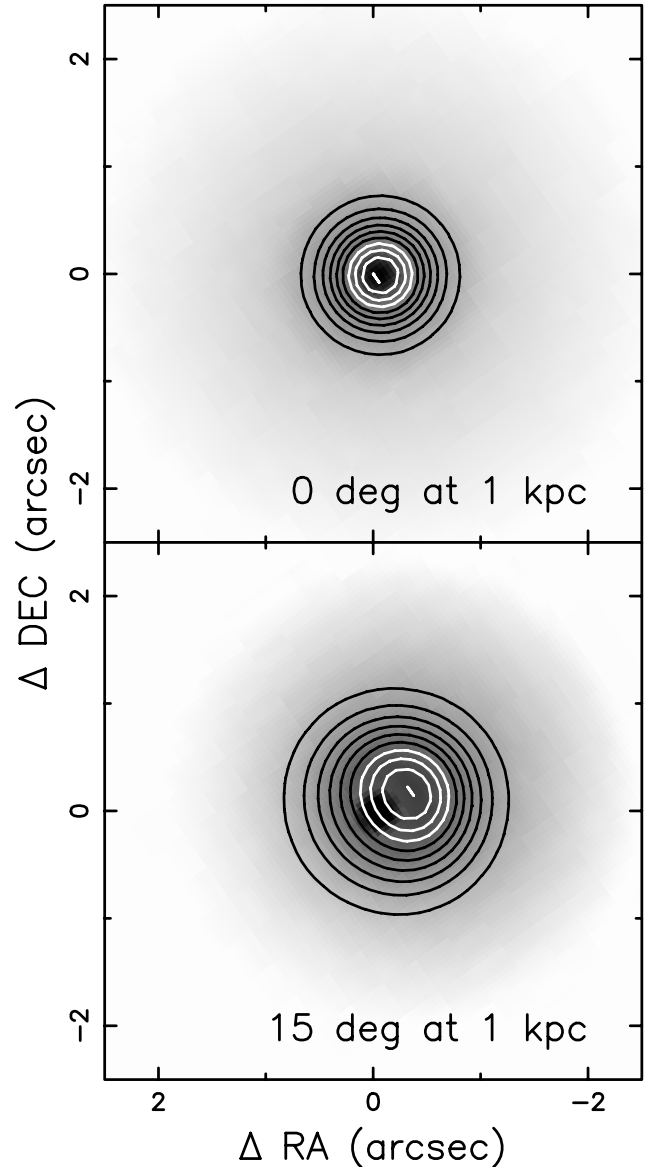


FIG. 8.—Model images for IRAS 17150–3224 rescaled for a distance of 1 kpc for comparison with HD 161796 images. Inclination angles of 0° and 15° shown. The contours show the thermal dust emission at $9.8 \mu\text{m}$, and the gray scale shows the optical B -band images.

tant in modifying the apparent morphology of PPNs, particularly the DUPLEX PPNs. Su, Hrivnak, & Kwok (2001) show the important effects of inclination angle on the appearance of PPNs that we would classify as DUPLEX PPNs. Inclination angle effects can cause an ambiguity in classifying a PPN as SOLE or DUPLEX if the PPN is viewed pole-on. Comparing the 0° images of Figures 4 and 7, we find little to distinguish the two subclasses in the optical or mid-IR images.

4.3. Evolution Effects

Evolutionary effects could also change appearances because these dust shells are expanding away from the central star and the optical depth of the dust shell is expected to decrease over time, changing an optically thick object like IRAS 17150 into one like HD 161796. We compute dynamical ages for each source by dividing the R_{\min} (Table 2)

parameter by the expansion velocity (v_{exp} ; Table 2) for each source. The dynamical ages for both objects, t_{dyn} (Table 2), are short but comparable. HD 161796 left the AGB ~ 300 yr ago. IRAS 17150 left 210 yr ago. Thus, there is little time for an object like IRAS 17150 to evolve into an object like HD 161796.

4.4. Dust Composition

One of the unanticipated results of our modeling was the significant difference in dust composition between HD 161796 and IRAS 17150. HD 161796 has mostly amorphous silicates but also crystalline silicates and crystalline water ice. In contrast, IRAS 17150 seems fitted adequately with just amorphous silicate, and recent *ISO* spectroscopy presented by Volk et al. (2001) shows no clear evidence for crystalline silicates. The grain sizes are remarkably different. IRAS 17150 has a wide range of grain sizes, with a minimum size of $0.001 \mu\text{m}$ and an effective maximum size of $200 \mu\text{m}$. HD 161796 has a narrower range of grain sizes, with a minimum size of $0.2 \mu\text{m}$ and an effective maximum size of $10.0 \mu\text{m}$. During our modeling efforts, we started with a single grain size, which proved to be inadequate, in particular for IRAS 17150. We also varied the a_{min} and a_0 values and found them to be quite sensitive ($\sim 10\%$ level) to the mid-IR and far-IR ends of the SED, respectively. While the exact values for a_{min} and a_0 are uncertain because of the inexactness of the dust composition, it is unlikely that this uncertainty is large enough to make the possible size distributions for these two objects the same.

The extremely large grain sizes found for IRAS 17150 are similar to those found for the Red Rectangle, another DUPLEX object, by Jura, Turner, & Balm (1997). Large grains were hypothesized to form in the long-lived disk of the Red Rectangle to explain their presence. It may be that IRAS 17150 also has a long-lived circumstellar disk. Our model certainly reveals an extreme equatorial density enhancement, which is essentially a disk. However, it is not clear if this disk is gravitationally bound to IRAS 17150 as it is with the Red Rectangle, and kinematic evidence is needed to establish such a fact.

Molster et al. (1999, 2000b, 2000c) have shown that PPNs with disks have stronger crystalline silicate band strengths than PPNs without disks, which they classify as outflow sources. In their studies, HD 161796 is considered an outflow source, which is independently supported by our model calculations. IRAS 17150 was not included in the studies by Molster et al. (1999, 2000b, 2000c). HD 161796 has crystalline silicates, while IRAS 17150 does not. Possibly, IRAS 17150 is early in its evolution and may develop prominent crystalline silicate bands as its central star evolves to hotter temperatures and the disk has time to evolve. In this scenario, large dust grains would evolve in the disk before the crystalline silicates. Alternatively, large grains may simply form when mass-loss rates are extraordinarily high because the higher densities may create environments conducive to growing large grains. In this scenario, crystalline silicates form as the disk evolves. It is also important to keep in mind that absence of evidence is not evidence of absence. Kemper et al. (2001) have shown that temperature differences between the amorphous and crystalline silicates can hide crystalline silicates in warm shells. In our model of IRAS 17150, the optical depth at $25 \mu\text{m}$ is ~ 7 , and it is possible that this high optical depth veils the crystalline silicate features.

4.5. Two Subclasses of PPNs

If our model calculations reflect a more general truth about PPNs, then there is a real physical difference between the DUPLEX and SOLE classes of PPNs suggested by Ueta et al. (2000). DUPLEX PPNs, such as IRAS 17150, originate from more massive progenitor stars than SOLE PPNs, such as HD 161796. DUPLEX PPNs experience more intensive and equatorially enhanced superwinds than SOLE PPNs. Detailed model calculations of several other PPNs by us and others (Meixner et al. 1997; Skinner et al. 1997; Su et al. 1998; Dayal et al. 1998; Ueta et al. 2001a) show similar general differences between SOLE and DUPLEX PPNs, as classified by Ueta et al. (2000). However, future detailed modeling of other PPNs may well reveal PPNs with physical parameters that fill in a spectrum where IRAS 17150 and HD 161796 mark the extreme end points.

We might expect there to be subclasses of PPNs because there are subclasses of PN morphologies, e.g., bipolar, elliptical, and round (Balick 1987; Manchado et al. 1996). Bipolar PNs originate from higher mass progenitors than elliptical PNs, as suggested by their differences in Galactic scale height (Corradi & Schwarz 1995). Higher mass star progenitors of PNs are expected to lose mass at higher rates because main-sequence stars initially of $0.8\text{--}8 M_{\odot}$ become white dwarfs, which have masses narrowly peaked at $0.6 M_{\odot}$ (Iben & Renzini 1983). Our model calculations presented here support the suggestion of Ueta et al. (2000) that DUPLEX and SOLE PPNs are precursors to bipolar and elliptical PNs, respectively.

The differences in mass-loss histories between DUPLEX PPNs (bipolar PNs) and SOLE PPNs (elliptical PNs) may also suggest that there is a difference in mass-loss mechanisms. Progenitor AGB stars of DUPLEX PPNs have a much more efficient means to lose their outer envelopes than SOLE PPN progenitors. It also appears that mass loss is more efficient when it is axisymmetric. Whether this mass-loss-enhancing process is interaction with a binary star companion or magnetic fields, a sudden increase in mass-loss rate coincident with an axisymmetric geometry must be explained.

5. CONCLUSIONS

Our radiative transfer models of HD 161796, a SOLE PPN, and IRAS 17150, a DUPLEX PPN, show that physical differences, not inclination angles, create their observed differences. HD 161796 and IRAS 17150 are both viewed nearly edge-on. However, IRAS 17150 experienced mass loss with a higher rate and with a higher equator-to-pole mass-loss ratio than HD 161796. This difference in mass-loss history created a larger optical depth of dust in IRAS 17150 than in HD 161796. If these calculations reflect a more general truth about PPNs, then they support the hypothesis put forth by Ueta et al. (2000) that SOLE PPNs and DUPLEX PPNs are physically distinct subclasses of PPNs. SOLE PPNs are probably descended from lower mass progenitor stars and are the precursors to elliptical PNs. DUPLEX PPNs are probably descended from higher mass progenitor stars and are the precursors to bipolar PNs. The dust compositions of both IRAS 17150 and HD 161796 are dominated by large amorphous silicate grains; however, the grain sizes have a much larger range for IRAS

17150 ($0.001 \mu\text{m} < a \lesssim 200 \mu\text{m}$), and HD 161796 contains a significant component of crystalline silicates and water ice.

We are grateful for the insightful comments of the referee, who gave the paper a very thorough review, and to M. Jura.

M. M., T. U., and A. S. are supported by NASA grants GO-06737.01-95A, GO-06364.02-95A, and STI 7898.02-96A, and NSF Career Award grant AST 97-33697. M. B. is supported by STScI grants GO-06364.01-94A and GO-006737.02-95A.

REFERENCES

- Balick, B. 1987, *AJ*, 94, 671
 Bertie, J. E., Labbé, H. J., & Whalley, E. 1969, *J. Chem. Phys.*, 50, 4501
 Blackman, E. G., Frank, A., & Welch, C. 2001, *ApJ*, 546, 288
 Burton, W. B. 1988, *Galactic and Extragalactic Radio Astronomy*, ed. G. L. Verschuur & K. I. Kellermann (Berlin: Springer), 295
 Collison, A., & Fix, J. 1991, *ApJ*, 368, 545
 Corradi, R. L. M., & Schwarz, H. E. 1995, *A&A*, 293, 871
 Dayal, A., Hoffmann, W. F., Biegging, J. H., Hora, J. L., Deutsch, L. K., & Fazio, G. G. 1998, *ApJ*, 492, 603
 Dominik, C., Sedlmayr, E., & Gail, H.-P. 1989, *A&A*, 223, 227
 Dorschner, J., Begemann, B., Henning, T., Jaeger, C., & Mutschke, H. 1995, *A&A*, 300, 503
 Draine, B. T., & Lee, H.-M. 1984, *ApJ*, 285, 89
 Fernie, J. D. 1983, *ApJS*, 52, 7
 Fernie, J. D., & Garrison, R. F. 1984, *ApJ*, 285, 698
 Frank, A., & Mellema, G. 1994, *ApJ*, 430, 800
 Garcia-Segura, G., Langer, N., Rozyczka, M., & Franco, J. 1999, *ApJ*, 517, 767
 Habing, H. J. 1996, *A&A Rev.*, 7, 97
 Habing, H. J., & Blommaert, J. A. D. L. 1993, in *Planetary Nebulae*, ed. R. Weinberger & A. Acker (Dordrecht: Kluwer), 243
 Hoogzaad, S. N., Molster, F. J., Dominik, C., Waters, L. B. F. M., Barlow, M. J., & de Koter, A. 2002, *A&A*, in press
 Hrivnak, B. J., & Kwok, S. 1991, *ApJ*, 371, 631
 Hrivnak, B. J., Kwok, S., & Volk, K. M. 1989, *ApJ*, 346, 265
 Hu, J. Y., Slijkuis, S., Nguyen-Q-Rieu, & de Jong, T. 1993, *A&A*, 273, 185
 Humphreys, R. M., & Ney, E. P. 1974, *ApJ*, 190, 339
 Iben, I., Jr. 1995, *Phys. Rep.*, 250, 2
 Iben, I., & Renzini, A. 1983, *ARA&A*, 21, 271
 Jaeger, C., Molster, F. J., Dorschner, J., Henning, T., Mutschke, H., & Waters, L. B. F. M. 1998, *A&A*, 339, 904
 Jura, M., Turner, J., & Balm, S. P. 1997, *ApJ*, 474, 741
 Justtanont, K., Barlow, M. J., Skinner, C. J., & Tielens, A. G. G. M. 1992, *ApJ*, 392, L75
 Justtanont, K., Skinner, C. J., Tielens, A. G. G. M., Meixner, M., & Baas, F. 1996, *ApJ*, 456, 337
 Kemper, F., Waters, L. B. F. M., de Koter, A., & Tielens, A. G. G. M. 2001, *A&A*, 369, 132
 Kim, S., Martin, P. G., & Hendry, P. D. 1994, *ApJ*, 422, 164
 Kwok, S. 1993, *ARA&A*, 31, 63
 Kwok, S., Hrivnak, B. J., & Geballe, T. R. 1995, *ApJ*, 454, 394
 Kwok, S., Hrivnak, B. J., Zhang, C. Y., & Langill, P. L. 1996, *ApJ*, 472, 287
 Kwok, S., Su, K. Y. L., & Hrivnak, B. J. 1998, *ApJ*, 501, L117
 Likkell, L., Morris, M., Omont, A., & Forveille, T. 1987, *A&A*, 173, L11
 Luck, R. E., Bond, H. E., & Lambert, D. L. 1990, *ApJ*, 357, 188
 Manchado, A., Guerrero, M. A., Stanghellini, L., & Serra-Ricart, M. 1996, *IAC Morphological Catalog of Northern Galactic Planetary Nebulae (La Laguna: IAC)*
 Mastrodomos, N., & Morris, M. 1998, *ApJ*, 497, 303
 Mathis, J. S., Ruml, W., & Nordsieck, K. H. 1977, *ApJ*, 217, 425
 Meixner, M., et al. 1999, *ApJS*, 122, 221
 Meixner, M., Skinner, C. J., Graham, J. R., Keto, E., Jernigan, J. G., & Arens, J. F. 1997, *ApJ*, 482, 897
 Molster, F. J., et al. 1999, *Nature*, 401, 563
 Molster, F. J., Waters, L. B. F. M., & Tielens, A. G. G. M. 2002a, *A&A*, 382, 222
 Molster, F. J., Waters, L. B. F. M., Tielens, A. G. G. M., & Barlow, M. J. 2002b, *A&A*, 382, 184
 Molster, F. J., Waters, L. B. F. M., Tielens, A. G. G. M., Koike, C., & Chihara, H. 2002c, *A&A*, 382, 241
 Neckel, T. H., Klare, G., & Sarcander, M. 1980, *A&AS*, 42, 251
 Neri, R., Kahane, C., Lucas, R., Bujarrabal, V., & Loup, C. A. 1998, *A&AS*, 130, 1
 Reddy, B. E., & Parathasarathy, M. 1996, *AJ*, 112, 2053
 Scott, A., & Duley, W. W. 1996, *ApJS*, 105, 401
 Servoin, J. L., & Piriou, B. 1973, *Phys. Status Solidi B*, 55, 677
 Skinner, C. J., et al. 1997, *A&A*, 328, 290
 Skinner, C. J., Meixner, M. M., Hawkins, G., Keto, E., Jernigan, J. G., & Arens, J. F. 1994, *ApJ*, 423, L135
 Soker, N. 1998, *ApJ*, 496, 833
 Su, K. Y. L., Hrivnak, B. J., & Kwok, S. 2001, *AJ*, 122, 1525
 Su, K. Y. L., Volk, K., & Kwok, S. 2000, in *ASP Conf. Ser. 199, Asymmetrical Planetary Nebulae II: From Origins to Microstructures*, ed. J. H. Kastner, N. Soker, & S. Rappaport (San Francisco: ASP), 159
 Su, K. Y. L., Volk, K., Kwok, S., & Hrivnak, B. 1998, *ApJ*, 508, 744
 Trammell, S. R., Dinerstein, H. L., & Goodrich, R. W. 1994, *AJ*, 108, 984
 Ueta, T., et al. 2001a, *ApJ*, 557, 831
 Ueta, T., Meixner, M., & Bobrowsky, M. 2000, *ApJ*, 528, 861
 Ueta, T., Meixner, M., Dayal, A., Deutsch, L. K., Fazio, G. G., Hora, J. L., & Hoffmann, W. F. 2001b, *ApJ*, 548, 1020
 van der Veen, W. E. C. J., Habing, H. J., & Geballe, T. R. 1989, *A&A*, 226, 108
 Volk, K. M., & Kwok, S. 1988, *ApJ*, 331, 435
 Volk, K., Kwok, S., Hrivnak, B., & Szczerba, R. 2001, in *Post-AGB Objects as a Phase of Stellar Evolution*, ed. R. Szczerba & S. K. Górný (Dordrecht: Kluwer), 323
 Warren, S. G. 1984, *Appl. Opt.*, 23, 1206
 Zuckerman, B., & Aller, L. 1986, *ApJ*, 301, 772